

Contents lists available at [ScienceDirect](#)

# Journal of Quantitative Spectroscopy & Radiative Transfer

journal homepage: [www.elsevier.com/locate/jqsrt](http://www.elsevier.com/locate/jqsrt)

## Cloud chamber laboratory investigations into scattering properties of hollow ice particles



Helen R. Smith<sup>a,\*</sup>, Paul J. Connolly<sup>a</sup>, Anthony J. Baran<sup>b</sup>, Evelyn Hesse<sup>c</sup>,  
Andrew R.D. Smedley<sup>a</sup>, Ann R. Webb<sup>a</sup>

<sup>a</sup> The University of Manchester, Oxford Road, Manchester M13 9PL, UK

<sup>b</sup> Met Office, Exeter, UK

<sup>c</sup> University of Hertfordshire, Hatfield, Hertfordshire, AL10 9AB

### ARTICLE INFO

#### Article history:

Received 2 May 2014

Received in revised form

15 February 2015

Accepted 16 February 2015

Available online 24 February 2015

#### Keywords:

Asymmetry parameter

Hollowness

Ice crystal

Ray Tracing

RTDF

Phase function

### ABSTRACT

Measurements are presented of the phase function,  $P_{11}$ , and asymmetry parameter,  $g$ , of five ice clouds created in a laboratory cloud chamber. At  $-7\text{ }^{\circ}\text{C}$ , two clouds were created: one comprised entirely of solid columns, and one comprised entirely of hollow columns. Similarly at  $-15\text{ }^{\circ}\text{C}$ , two clouds were created: one consisting of solid plates and one consisting of hollow plates. At  $-30\text{ }^{\circ}\text{C}$ , only hollow particles could be created within the constraints of the experiment. The resulting cloud at  $-30\text{ }^{\circ}\text{C}$  contained short hollow columns and thick hollow plates. During the course of each experiment, the cloud properties were monitored using a Cloud Particle Imager (CPI). In addition to this, ice crystal replicas were created using formvar resin. By examining the replicas under an optical microscope, two different internal structures were identified. The internal and external facets were measured and used to create geometric particle models with realistic internal structures. Theoretical results were calculated using both Ray Tracing (RT) and Ray Tracing with Diffraction on Facets (RTDF). Experimental and theoretical results are compared to assess the impact of internal structure on  $P_{11}$  and  $g$  and the applicability of RT and RTDF for hollow columns.

© 2015 The Authors. Published by Elsevier Ltd. This is an open access article under the CC BY license (<http://creativecommons.org/licenses/by/4.0/>).

### 1. Introduction

The role of clouds in the Earth's radiation budget is still considered one of the biggest uncertainties in predicting climate change today [1]. Ice clouds are of particular interest as the large range of ice crystal size, shape and complexity gives rise to considerable variabilities in their net radiative effect [2–4]. In addition to this, cirrus has an

extensive global coverage of 30%, with coverage in the tropics reaching 60–70% [5].

Ice crystal habit has been an area of scientific curiosity for centuries [6–8], with many studies of natural snow crystals noting the wide variety of crystal morphologies. In the 1930s, the first controlled laboratory investigations into crystal habit were conducted, where crystal growth was observed over a variety of conditions [9]. These findings were presented in the form of a morphology diagram, describing ice crystal habit as a function of temperature and supersaturation. Since then, observations from numerous laboratory and field studies have built on the original morphology diagram, with several other particle habits discovered over a larger range of

\* Corresponding author.

E-mail address: [helen.smith-8@postgrad.manchester.ac.uk](mailto:helen.smith-8@postgrad.manchester.ac.uk) (H.R. Smith).

temperatures and supersaturations [10,11]. In order to identify ice crystal habit, laboratory based experiments have used a variety of techniques including photography, formvar replicas, and cloud probes [12–16]. Although some in situ studies have used replication techniques [17,18], in situ habit information is mostly gathered with the use of 2D imaging probes such as the Stratton Park Engineering Company (SPEC) Cloud Particle Imager (CPI) (see Section 2.2.1) [19]. The CPI is capable of determining the habits and sizes of particles in the size range 10–2000  $\mu\text{m}$  and as such it has been used in determining the habit and size distributions of various cloud types in several field experiments [18–26]. However, the ability to accurately determine habit from CPI images is hampered by particle orientation and the limited resolving power of the probe.

The variety in particle size and shape poses many challenges in the modelling of scattering by ice crystals. Multiple studies have highlighted the importance of crystal habit upon the scattering properties [27–34]. Simplified shapes such as cylinders and spheroids were found to be inadequate approximations [35], and the more accurate simple hexagonal column still predicts higher asymmetry parameters and more prominent halo features than those observed from satellite and aircraft data [36–41]. The featureless phase functions are known to be related to crystals with mesoscopic surface roughness, aggregates and particles with inclusions. Consequently, surface roughness and internal structure have gained recognition as important factors in the scattering properties of ice crystals [42–47]. These small scale features cannot be accurately determined from cloud probe images and consequently may be overlooked in particle models. Although approximations to observed surface roughness are often used, details of the inclusions have yet to be accounted for in particle models since suitable measurements have not previously been available.

There have been a number of theoretical studies of idealized surface roughness. By creating rough surfaces in the particle model by tilting facet mantles, or by distorting the outgoing ray paths, results from these studies agree that ice particle roughness leads to a general decrease in asymmetry parameter in addition to a more featureless phase function [31,48]. However, a recent paper showed that the mantle tilting method does not replicate idealized surface roughness for high values of roughness [49]. Experimental difficulties mean that direct measurements of ice surface roughness are scarce. In general, the surface roughness of ice crystals is beyond the capabilities of optical microscopy, and the coating techniques required for electron microscopy mean that the ice surface cannot be directly imaged. Recently, however, the Variable Pressure Scanning Electron Microscope (VP-SEM) has proved successful in measuring ice surface roughness [50]. One study used the Small Ice Detector version 3 (SID-3) to obtain two-dimensional scattering patterns from ice crystals [51]. By making use of the relationship between surface energy and roughness, these scattering patterns may be used to estimate ice crystal roughness. This technique has the ability to distinguish between particles of varying degrees of roughness and has been used in situ for the classification of naturally occurring ice crystals [45].

Similar to surface roughness, internal structure is also known to influence the scattering properties of ice crystals. One theoretical study modelled cavities using hexagonal based pyramids which were identified by CPI particle images [52]. Ray Tracing results from these models showed a reduction in asymmetry parameter for hollow particles at certain aspect ratios. Another study used a similar particle model based on photomicrograph images of hollow rosettes at the South Pole [53]. In their study, a more rigorous physical optics approach was used which showed a general increasing trend in the asymmetry parameter for hollow particles [53]. Both these studies used comparable internal structures based on different particle images. Similar indentations can be seen from a number of experiments [10,54]. Other sources show varied and complex cavities [17,55], the structure of which are difficult to determine using two-dimensional images and may be missed entirely with instruments of limited resolution. This results in over-idealized geometries being used for hollow ice crystals in particle models. As the single scattering properties are known to be sensitive to particle habit, it is probable that the faithful representation of internal geometry is also necessary. Further laboratory investigations are therefore pivotal in determining internal structure and its impact upon the single scattering properties, and to test light scattering models.

## 2. Experimental set-up

### 2.1. Cloud chamber

The experiments presented in this paper were conducted in the Manchester Ice Cloud Chamber (MICC), as previously described [56]. The cloud chamber consists of a 10 m tall fall tube of 1 m diameter. The chamber is housed in three stacked cold rooms capable of reaching temperatures down to  $-55\text{ }^{\circ}\text{C}$ . The set-up used in this experiment is shown in Fig. 1.

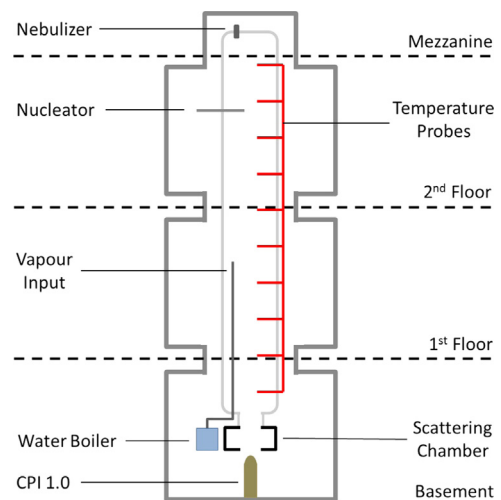


**Fig. 1.** Schematic of the Manchester Ice Cloud Chamber. A 10 m tall fall tube is housed in three cold rooms over three stories. Various access points allow the addition of liquid water and vapour, and a compressed air line is used to nucleate ice in the cloud.

At the top of the chamber, a Schlick Form 5 two-substance nebulizer was used to create a cloud of supercooled liquid water droplets. The micrometer scale on the nebulizer allowed the size and concentration of water droplets to be controlled. Approximately 1 m below the nebulizer, ice was nucleated in the cloud using a compressor expansion technique [16,57,56]. To employ this technique, a solenoid valve was used to open and close a compressed air line. When the valve was opened, the compressed air expanded adiabatically, thus cooling the local environment to below the homogeneous nucleation temperature and forcing the formation of ice. In these experiments, the solenoid valve was opened and closed periodically in order to provide a steady flux of ice nuclei. Water vapour was input at the midpoint of the chamber via a water boiler, therefore the ice crystals continued to grow as they fell through the chamber. All experiments were conducted at ambient atmospheric pressure (1010 mbar).

It is known from previous studies that the ice crystal habit is dependent on temperature and supersaturation [9,10]. From certain habit diagrams, it is clear that certain temperature ranges produce particular habits [58]. It is also evident that the ice crystal structure becomes more complex with increasing supersaturation, allowing for the formation of hollow columns and sectored plates above water saturation. Therefore, in order to create a variety of solid and hollow habits in the ice cloud chamber, the temperature and humidity had to be altered. The temperature of the chamber was set and maintained by selecting the cold room temperatures. The temperature inside the chamber was found to be stable within  $\pm 1.5^\circ$ . However, the supersaturation is dependent upon a number of factors and could not be as easily constrained. Two methods were used to vary the supersaturation: changing the ice crystal concentration, and altering the vapour input. By decreasing the ice crystal concentration, or by increasing the amount of water vapour, the supersaturation was increased. The ice crystal concentration was controlled by the droplet input and the nucleator frequency, whereas the vapour input was controlled by a variable power supply. By altering these inputs, clouds of predominantly hollow or particles were achieved. Using this experimental set-up, the profile of the cloud was vertically inhomogeneous inside the chamber and therefore representative measurements of relative humidity could not be taken.

## 2.2. Cloud measurement

### 2.2.1. CPI

Inside the scattering section (described in Section 2.3), a Cloud Particle Imager (CPI) samples the cloud as it falls out of the chamber [59]. The CPI has been used in numerous laboratory and field studies [22,60,61]. The probe takes 2D images of the ice crystals which are then processed using CPIview. CPIview gives information on particle size, habit and concentration. In these experiments, the CPI was used to monitor ice crystal concentration.

### 2.2.2. Ice crystal replicas

In addition to the CPI, the cloud was monitored using ice crystal replicas. These are made using a 0.6% solution of

polyvinyl formal ( $C_3H_7$ ), commonly known as formvar, in chloroform. This solution was chilled in the cold room prior to collecting samples. The solution was applied to microscope slides which were placed in the cloud chamber to collect falling ice crystals. The slides were left to dry in a sealed bell jar filled with desiccant in order to minimise the production of artefacts. The ice crystals which fall on the microscope slide are encompassed by the formvar solution, as the chloroform evaporates, the ice crystal is preserved in a formvar shell [62]. Once dry, the ice crystal replicas were examined under an optical microscope. The dimensions of both internal and external facets were measured using a microscope graticule. These measurements were used to construct geometric particle models with realistic internal structures, discussed in Section 3.

## 2.3. Scattering chamber

The scattering experiments were conducted in a separate scattering chamber, which was attached to a sampling port at the bottom of the cloud chamber. Fig. 2 shows a cross-sectional view of the scattering chamber.

The scattering chamber has been previously described in several papers [57,16,15]. However, a brief description is given here. The chamber is a cylindrical enclosure of diameter 0.45 m and height 0.3 m. A 0.3 m opening at the top of the scattering chamber attaches to the bottom of the cloud chamber, and an opening at the bottom allows the cloud to fall through freely. The lasers are mounted outside the chamber in a temperature controlled box, and the beams are directed through the centre of the chamber. The base of the scattering chamber contains a motor controlled rotating platform with an angular resolution of  $0.19^\circ$  per step. The detector optics were mounted on the rotating platform in the same plane as the lasers, at a distance of 0.06 m from the centre of the scattering section. Consequently, the measured intensities are considered to be in the far-field.

## 2.4. Optical set up

The optical set-up is shown via a plan view of the scattering chamber in Fig. 3.

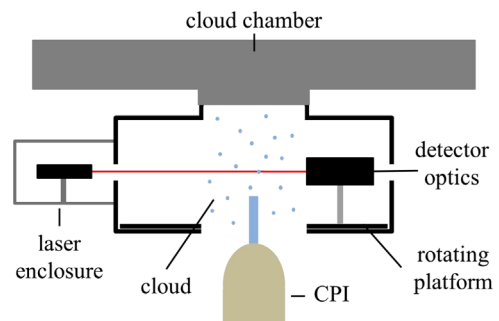


**Fig. 2.** Vertical cross-sectional schematic of the scattering chamber. The laser is directed through the cylindrical cloud of diameter 0.3 m. The detector optics rotate around the central axis of the cloud, collecting scattered light.

The experiment used two 5 mW diode lasers: a Taurus 635 nm red laser, and an Electra portable 405 nm violet laser, both manufactured by Laserglow Technologies. The degree of polarization of the red and violet lasers were measured to be 0.91 and 0.87 respectively. The lasers were oriented so they were linearly polarized at  $45^\circ$  to the scattering plane.

The intensities of the red and violet lasers were monitored over experimental temperatures for several hours in order to determine the stability of the power of the input beam. The intensities were measured to be stable within 3.1% and 2.8%, respectively. The divergence of the red and violet beams was measured to be  $<1.2$  mrad and  $<0.5$  mrad, respectively. As the maximum path length of each laser was  $<0.3$  m, the divergence of the lasers was not further considered. The detector optics had a field of view of  $1.0^\circ$ , as the distance from the detector optics to the centre of the scattering volume was  $<0.06$  m, this divergence was also considered negligible and was not further considered.

In order to utilize both wavelengths in each experiment, the lasers were directed through the centre of the

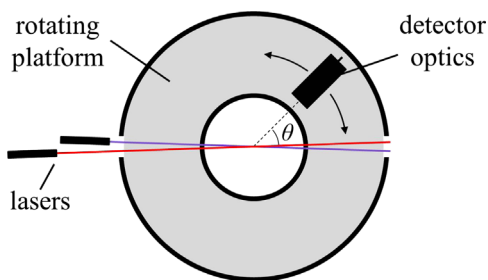


**Fig. 3.** Plan view of the optical set-up. The grey disc represents the rotating platform at the bottom of the scattering chamber, the detector optics were fixed onto this. The detector rotated around a vertical axis at the centre of the chamber, and hence the centre of the cloud (not to scale).

scattering section, separated by an angle of  $0.94^\circ$  (five steps) as shown in Fig. 3. By offsetting them in this way, the scattered intensity could then be measured for each laser simultaneously, although the red and violet signals corresponded to different scattering angles. The detector optics consisted of a planoconvex lens with a focal length of 0.10 m. A fibre optic was placed at the focal length, and a collar was placed before the lens, restricting the field of view to  $1.0^\circ$ . The detector optics fed into an Ocean Optics S2000 CCD array spectrometer which measured the intensity of the scattered light. The spectrometer has a wavelength range of 200–850 nm over 2048 pixels. The low dynamic range of the instrument required the additional use of neutral density filters to record high intensities in the  $0$ – $10^\circ$  range. Beyond this, the integration time of the instrument was altered in order to measure varying intensities of scattered light. Corrections for filters, integration time and dark current are applied in post processing.

#### 2.4.1. Measurements

Each measurement was taken over the course of a minute and therefore corresponds to an ensemble of particles passing through the scattering volume. During each measurement, the detector was stationary. It was then moved five steps and the next measurement was taken. This process was repeated every  $0.95^\circ$  between angles  $0.38^\circ$  and  $150.4^\circ$ ; beyond this, the detector optics intersected the laser beam and thus no useful data could be collected for  $\theta > 150^\circ$ . The measured intensity corresponds to a scattering volume,  $V$ , defined in this paper as the volume of the laser which falls within the field of view of the detector optics (shown in Fig. 4).

The scattering volume changes depend upon the position of the detector, and is therefore a function of angle,  $\theta$ , where  $\theta$  is the angle subtended by the straight through beam and the detector optics. Only light scattered within this volume is seen by the detector optics and as such the measured

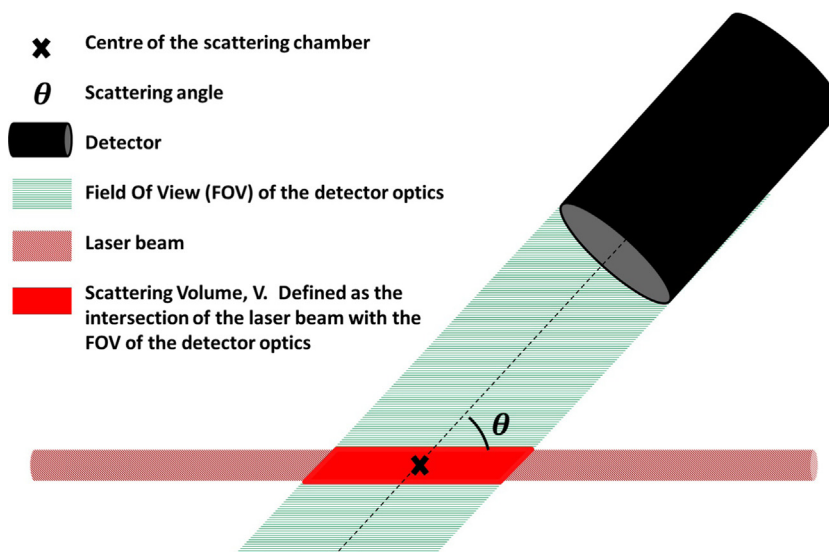


**Fig. 4.** The scattering volume,  $V$ , is the volume in which the laser intersects the field of view of the detector optics. Only light scattered in the plane of the detector optics from within the scattering volume is observed. The measured signal is therefore proportional to  $V$ , which is a function of scattering angle,  $\theta$ .

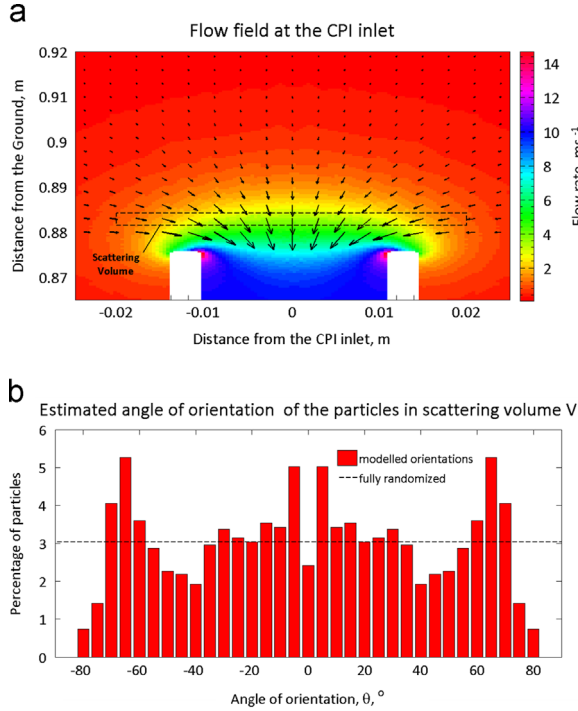


**Fig. 5.** Modelled flow field at the CPI inlet and estimated ice crystal orientations, expressed as the angle the major axis of the ice crystal makes to the horizontal.

intensity is proportional to  $V$ . In order to correct for this, the measured intensity is divided by the scattering volume in order to get the scattered intensity per unit volume.

### 2.5. Particle orientation

Ice particles are observed to fall preferentially with their major axis perpendicular to direction of propagation [63,64]. The amount by which they deviate from this orientation can be described by the tilt angle. As particles become larger and more elongated, the tilt angles decrease and the particles become more preferentially oriented.

The flow field inside the scattering volume was modelled using the Partial Differential Equation toolbox in Matlab 2014b. In order to do this, the cold room environment was modelled using Neumann boundary conditions for solid objects and Dirichlet conditions for the inlet tube to the CPI, which had a known flow speed. In these experiments, the inlet tube to the CPI lies  $\sim 1$  cm below the scattering volume (Fig. 4). The resultant flow field is shown in Fig. 5a. The average ice crystal fall speeds were estimated to be  $\sim 0.25$   $\text{ms}^{-1}$  [65]. The net movement of the crystal is then approximated by adding the velocities of the flow field to the crystal fall speeds. Assuming that the major axis of the ice crystal is oriented orthogonal to the direction of propagation, the deviation of the axis or orientation from the horizontal is estimated. These angular deviations are estimated to be between  $-81^\circ$  and  $81^\circ$ , the distribution of orientations is shown in Fig. 5b. It was also assumed that the ice crystals maintain a rotational degree of freedom about their minor axis. Other factors such as

ambient shears are likely to cause additional deviations from the estimated orientation. For the purposes of this experiment, orientation was treated as random.

### 2.6. Obtaining the scattering phase function, $P_{11}$

The red and violet lasers are partially linearly polarized at an angle of  $45^\circ$  to the scattering plane. The degree of polarization of each laser was measured to be 0.91 and 0.87. Therefore the incident Stokes parameters are given by

$$I_{0(v)} \begin{bmatrix} 1 \\ 0 \\ p_v \\ 0 \end{bmatrix} \quad \text{and} \quad I_{0(r)} \begin{bmatrix} 1 \\ 0 \\ p_r \\ 0 \end{bmatrix}$$

where  $I_{0(v)}$  is the intensity of the violet laser,  $\text{W m}^{-2}$ ;  $I_{0(r)}$  is the intensity of the red laser,  $\text{W m}^{-2}$ ;  $p_v$  is the degree of polarization of the violet laser;  $p_r$  is the degree of polarization of the red laser.

In order to calculate the Stokes parameter of the scattered wave, we assume that the particles in the scattering volume are randomly oriented, as discussed in Section 2.5. By making this assumption, the Stokes parameter of the scattered wave can be given by [66]

$$\begin{bmatrix} I \\ Q \\ U \\ V \end{bmatrix} = \frac{I_0}{k^2 r^2} \begin{bmatrix} P_{11} & P_{12} & 0 & 0 \\ P_{12} & P_{22} & 0 & 0 \\ 0 & 0 & P_{33} & P_{34} \\ 0 & 0 & -P_{34} & P_{44} \end{bmatrix} \begin{bmatrix} 1 \\ 0 \\ p \\ 0 \end{bmatrix} \quad (1)$$

where  $I_0$  is the intensity of the incident beam,  $\text{W m}^{-2}$ ;  $k$  is the wavenumber;  $r$  is the distance from the scattering particle to the detector, m

$$\begin{bmatrix} I \\ Q \\ U \\ V \end{bmatrix} = \frac{I_0}{k^2 r^2} \begin{bmatrix} P_{11} \\ P_{12} \\ p \times P_{33} \\ -p \times P_{34} \end{bmatrix} \quad (2)$$

and therefore

$$I \propto P_{11} \quad (3)$$

where  $I$  is the total scattered intensity as a function of angle  $\theta$ . Therefore the measured intensities described in Section 2.4 can be normalised to  $4\pi$  in order to obtain the phase function  $P_{11}$ , according to

$$\int_0^\pi P_{11}(\theta) \sin \theta d\theta = 2 \quad (4)$$

As we cannot measure beyond  $\theta = 150.4^\circ$ , modelled data were used to fill in the range  $150.4$ – $180^\circ$ . Images of the formvar replicas were analysed in order to create suitable particle models for each cloud. In all experiments, it was found that each cloud consisted of only one crystal habit, although the aspect ratio was found to change with particle size. Here, the aspect ratio is defined as the ratio of the length of the prism face to the length of the basal face. Particles with an aspect ratio  $> 1$  are considered to be column-like, whereas particles with an aspect ratio  $< 1$  are considered to be plate-like. A habit mixture model was created that was based on one habit but several sizes and aspect ratios. Details of the composition of each cloud can

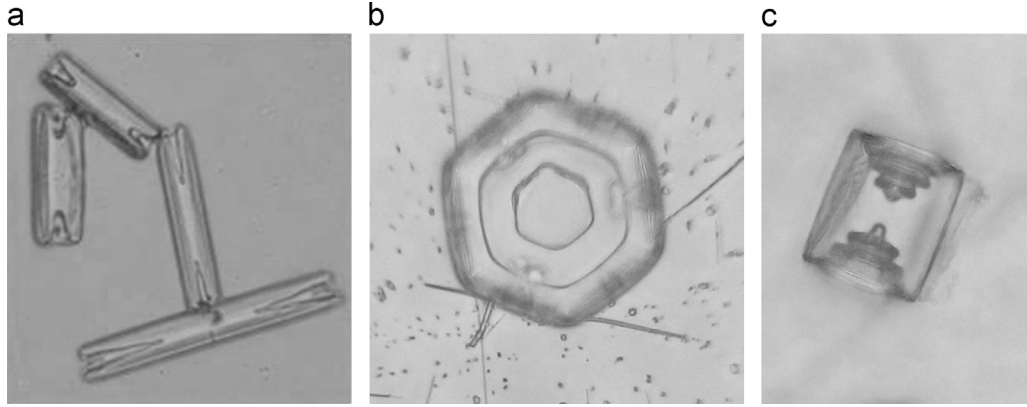


Fig. 6. Formvar replicas showing typical structures of hollow particles at (a)  $-7\text{ }^{\circ}\text{C}$ , (b)  $-15\text{ }^{\circ}\text{C}$  and (c)  $-30\text{ }^{\circ}\text{C}$ .

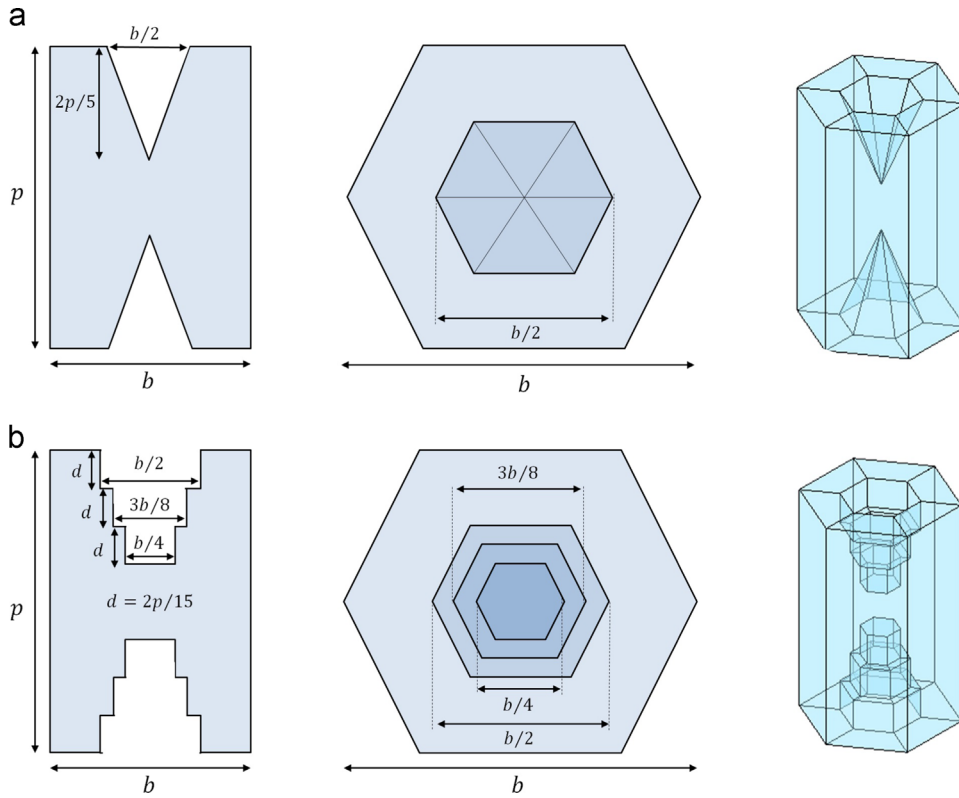


Fig. 7. Construction of the particle models based on formvar replicas. (a) Shows the construction of a typical hollow column as observed at  $-7\text{ }^{\circ}\text{C}$  and (b) shows the construction of a typical hollow column as observed at  $-30\text{ }^{\circ}\text{C}$ . From left to right: cross sectional view taken parallel to the prism face, plan view as seen from the basal face, and 3D model.

be found in Section 3. Both Ray Tracing [31] and RTDF were tested (see Section 3.1). RTDF differs from conventional geometric optics by considering diffraction at facets in addition to diffraction at the projected cross-section. Therefore, RTDF better describes the size dependence, especially for small and intermediate size parameters [67]. RTDF phase functions were used to normalise the measured results. The data were normalised as follows:

$$f \times \int_0^{150.4^{\circ}} I_{sca}(\theta) \sin \theta \, d\theta + \int_{150.4^{\circ}}^{180^{\circ}} m(\theta) \sin \theta \, d\theta = 2 \quad (5)$$

where  $m(\theta)$  is the modelled data and  $f$  is a scaling factor required to normalise the phase function. The normalised intensity,  $I_{sca}(\theta) \times f$ , is then plotted as a function of  $\theta$ . The asymmetry parameter,  $g$ , is defined as

$$g = \frac{1}{2} \int_0^{180^{\circ}} P_{11}(\theta) \sin \theta \cos \theta \, d\theta \quad (6)$$

For the measured phase functions, the asymmetry parameter was found by using  $P_{11} = I_{sca}(\theta) \times f$  in the range  $\theta = 0.38\text{--}150.4^{\circ}$  and using the modelled values of  $P_{11}$  in the range  $\theta = 150.4\text{--}180^{\circ}$ .

3. Results

3.1. Theoretical results

Measurements from the formvar replicas (Fig. 6) were used to create geometric models, which represented internal structure.

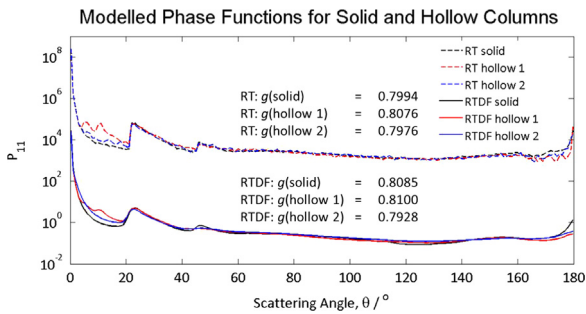


Fig. 8. Ray Tracing and RTDF results for solid columns and both types of hollow columns. ‘Hollow 1’ denotes the typical hollow structure as seen at  $-7^{\circ}\text{C}$ , as depicted in Fig. 7a. ‘Hollow 2’ denotes the typical hollow structure as seen at  $-30^{\circ}\text{C}$ , as depicted in Fig. 7b. The results from Ray Tracing are offset by  $10^4$  in order to present both models on the same graph.

Table 1

Modelled asymmetry parameters for solid columns and both types of hollow columns for a prism length of  $100\ \mu\text{m}$  and a basal length of  $50\ \mu\text{m}$ . ‘Hollow 1’ corresponds to the typical internal structure seen at  $-7^{\circ}\text{C}$ , and ‘Hollow 2’ corresponds to the typical internal structure seen at  $-30^{\circ}\text{C}$ , ‘% dev.’ gives the percentage deviation of the modelled asymmetry parameter of the hollow models from the modelled asymmetry parameter of the solid models.

Model	Ray Tracing		RTDF	
	$g$	% Dev.	$g$	% Dev.
Solid	0.7994		0.8085	
Hollow 1	0.8076	1.03	0.8100	0.12
Hollow 2	0.7976	-0.23	0.7928	-1.94

Experiments at  $T = -7^{\circ}\text{C}$  and  $T = -30^{\circ}\text{C}$  both produced columnar habits in agreement with established habit diagrams [10]; however, there were notable differences between the columns grown at  $-30^{\circ}\text{C}$  and the columns grown at  $-7^{\circ}\text{C}$ . At  $-30^{\circ}\text{C}$  (Fig. 6c) the columns showed a stepped internal structure. Whereas at  $-7^{\circ}\text{C}$  (Fig. 6a) the columns showed a simpler internal structure.

When viewed from the basal face, each indentation of the stepped hollow column had hexagonal symmetry. Based on averaged measurements, each indentation was constructed by three hexagonal columns of descending size. The size of the basal faces is measured as  $b/2$ ,  $3b/8$  and  $b/4$ , where  $b$  is the length of the basal facet of the ice crystal. The depth of each indentation is measured as  $2p/15$  where  $p$  is the length of the prism facet of the ice crystal. The columns created at  $-7^{\circ}\text{C}$  could not be viewed from the basal face due to the tendency of the ice crystals to lie with their prism facets parallel to the microscope slide. It was assumed that these indentations also retained hexagonal symmetry and therefore they were modelled using hexagonal based pyramids. Each indentation had a base width of  $b/2$  and a height of  $2p/5$ . At  $-15^{\circ}\text{C}$  the plates (Fig. 6b) could not be viewed from their prism face due to their orientation. Although the thickness of the plates could be estimated using CPI images, the vertical profile of the internal structure could not be investigated

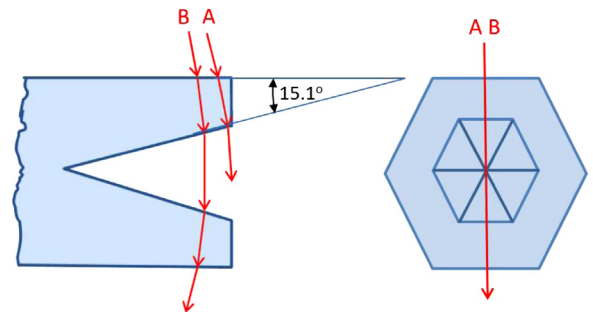


Fig. 9. Schematic of ray paths causing additional halos in hollow column 1 compared to a solid column:  $\sim 4.7^{\circ}$  (path A),  $\sim 9.5^{\circ}$  (path B).

Ratios of RT phase functions to RTDF phase functions for solid and hollow columns

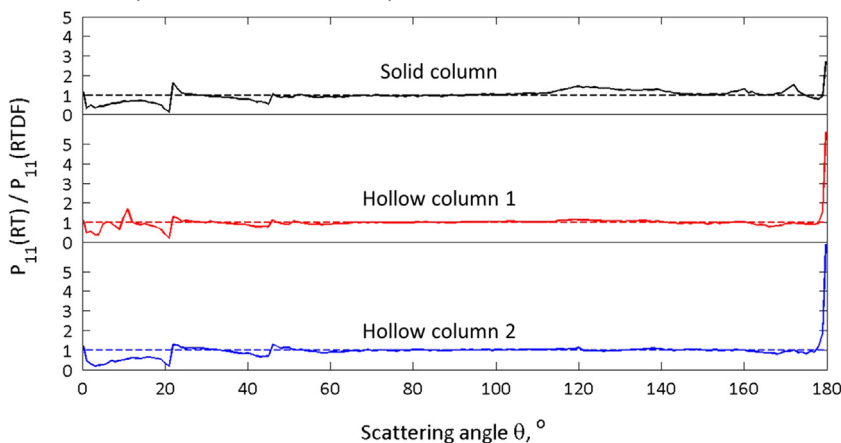


Fig. 10. Ratios of the RT phase functions to RTDF phase functions for solid and hollow columns.

in detail. From the formvar images, the internal structure of plates appeared similar to the structure of the stepped columns seen at  $-30^{\circ}\text{C}$ , although the structure became increasingly complex as the plates increased in size. For this reason, plates were modelled using the same geometry as the stepped column with a thickness of  $15\ \mu\text{m}$  based on observations from the CPI.

3.1.1. Results from Ray Tracing and Ray Tracing with Diffraction on Facets

Three example columns were constructed in order to directly compare the effects of each indentation: one solid column, one hollow column with a pyramidal cavity (as observed at  $-7^{\circ}\text{C}$ ), and one hollow column with stepped internal structure (as observed at  $-30^{\circ}\text{C}$ ). Each column measured  $100\ \mu\text{m}$  (prism face) by  $50\ \mu\text{m}$  (basal face), and each indentation measured  $40\ \mu\text{m}$  in depth. The phase function and asymmetry parameter were found using both

Ray Tracing and RTDF, for a wavelength of  $635\ \text{nm}$  and a complex refractive index of  $1.3085 + (1.04 \times 10^{-8})i$  [68]. All modelled results presented in this paper are based on random orientations. Results using the two methods are presented in Fig. 8 and Table 1.

Comparing the RT and RTDF results in Fig. 8, one notable difference is the increased scattering between about  $3^{\circ}$  and  $20^{\circ}$  observed for hollow column 1. The phase function of hollow column 1 has two additional peaks at  $\sim 4.7^{\circ}$  and  $9.5^{\circ}$ , which are due to ray paths sketched in Fig. 9. Ray path A corresponds to the halo for the prism angle of  $15.14^{\circ}$ . Path B is similar, but the ray re-enters the crystal and goes through a second deflection. Therefore, the complete deflection angle is about twice the deflection angle for ray path A. This increase in forward scattering leads to a noticeably higher for hollow column 1 when compared with the solid column. Due to the stepped indentation of hollow column 2, which only includes additional  $90^{\circ}$  prism angles, there is only a small increase in forward scattering compared to the solid column. In this case, the reduction in the  $22^{\circ}$  halo, in addition to the increase in scattering in the  $120\text{--}140^{\circ}$  region leads to an overall decrease in asymmetry parameter. Therefore, the asymmetry parameter of hollow column 2 is rather similar to that of the solid column.

To compare the two scattering models, the ratios of the RT phase functions to the RTDF phase functions are plotted in Fig. 10. The RTDF phase functions are similar to RT; however, the peaks are broadened due to diffraction on facets. Due to this, some of the intensity of the  $22^{\circ}$  halo peak is moved towards smaller scattering angles. For all particles, scattering close to  $180^{\circ}$  is significantly smaller for

Table 2  
Summary of input parameter and cloud properties for each experiment.

Experiment	Temperature ( $^{\circ}\text{C}$ )	Ice crystal concentration ( $\text{l}^{-1}$ )	Predominant habit	Size range ( $\mu\text{m}$ )
1	$-7$	10,000	Solid column	10–170
2	$-7$	2500	Hollow column	20–280
3	$-15$	5000	Solid plate	10–290
4	$-15$	1000	Hollow plate	20–290
5	$-30$	1000	Hollow plate/ columns	10–140

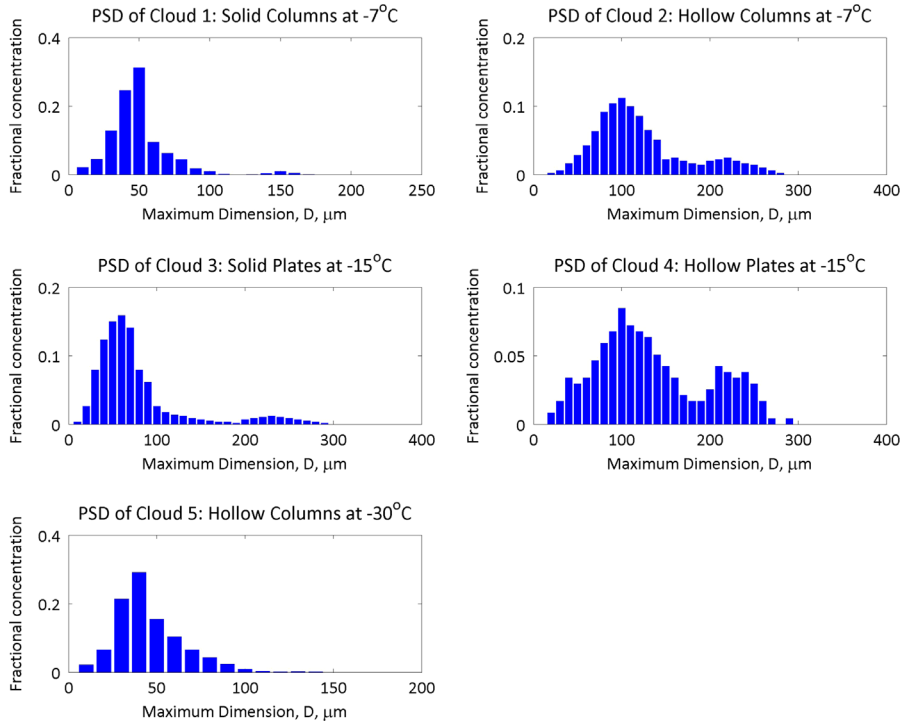
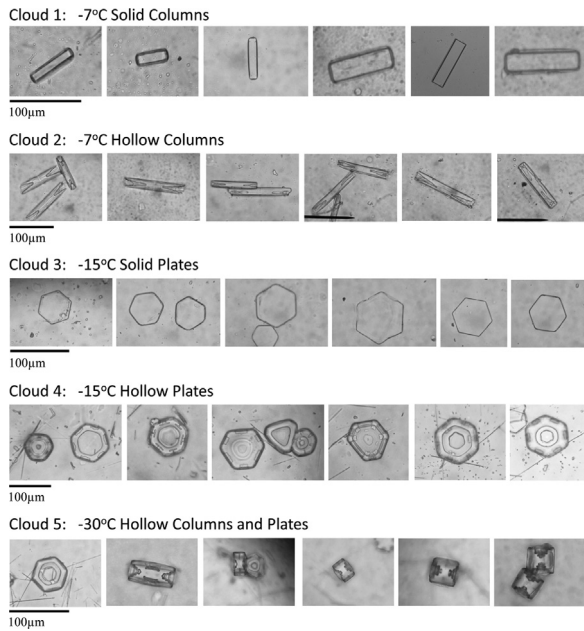
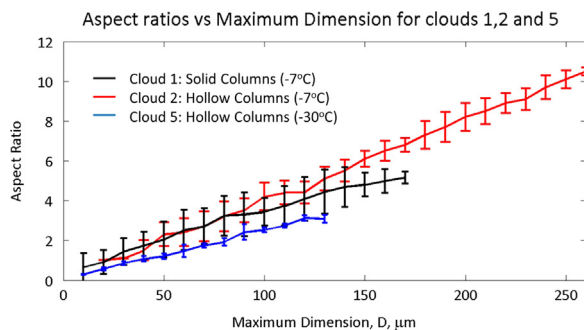


Fig. 11. Particle size distributions for the five clouds created during these experiments. Approximately 1000 formvar images were analysed for each cloud.



**Fig. 12.** Formvar replicas showing typical habits observed during the five experiments.



**Fig. 13.** Aspect ratios of hollow and solid columns based on measurements from formvar replicas.

RTDF when compared with RT, particularly in the case of the hollow columns. Overall, these deviations result in a 1.4% increase in the RTDF predicted asymmetry parameter for the solid column when compared to RT. For hollow column 1, RTDF predicts an asymmetry parameter 0.12% larger than RT. This increase is rather small, which is most likely due to a reduction of the RTDF forward scattering peak at  $\theta = 0.25^\circ$  because of the smaller area of parallel basal facet components. The RTDF forward scattering peak is slightly more reduced for hollow column 2 when compared with RT, presumably due to the segmentation of the basal facets into smaller components causing stronger diffraction as well as additional ray paths. This results in a 2% lower asymmetry parameter for hollow column 2 compared to the solid column when using RTDF.

### 3.2. Experimental results

Five experiments were conducted. In order to produce different habits, several input variables were changed.

Measured and Modelled Phase Functions for a  $-7^\circ\text{C}$  Cloud of Solid Columns

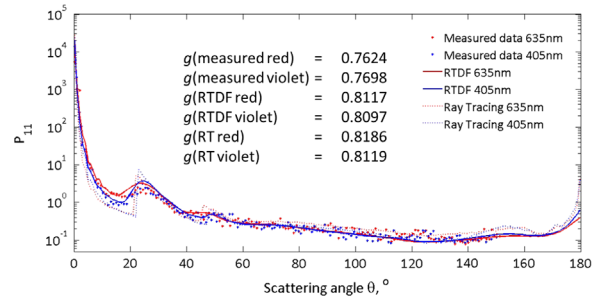


**Fig. 14.** Measured and modelled phase functions for solid columns at  $-7^\circ\text{C}$ .

Measured and Modelled Phase Functions for a  $-7^\circ\text{C}$  Cloud of Hollow Columns

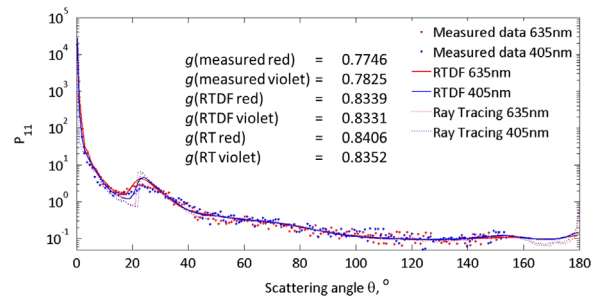


**Fig. 15.** Measured and modelled phase functions for hollow columns at  $-7^\circ\text{C}$ .

Measured and Modelled Phase Functions for a  $-15^\circ\text{C}$  Cloud of Solid Plates

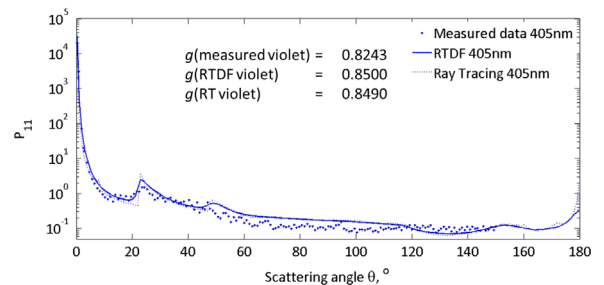


**Fig. 16.** Measured and modelled phase functions for solid plates at  $-15^\circ\text{C}$ . Intensity measurements from the red laser are unavailable for this experiment.

Three temperatures were chosen in order to cover different habit regimes. Ice crystal concentration and vapour input were varied in order to alter the relative humidity in the chamber. The input parameters are summarised in Table 2.

#### 3.2.1. Particle size distributions

Particle size distributions were measured from the formvar replicas. These results are presented in Fig. 11.

#### 3.2.2. Particle habits

The formvar replicas were also used to determine the particle habits. It was found that each cloud consisted of one particle habit, with a range of sizes and aspect ratios. Typical particle habits are shown in Fig. 12.

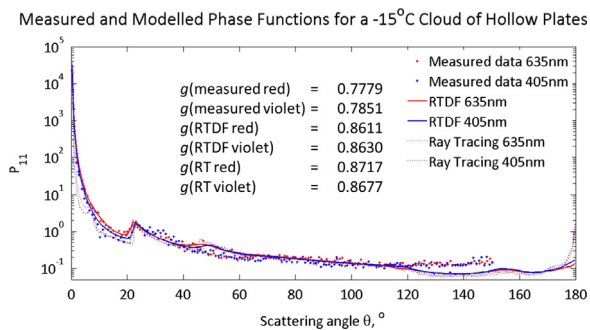


Fig. 17. Measured and modelled phase functions for hollow plates at  $-15^{\circ}\text{C}$ .

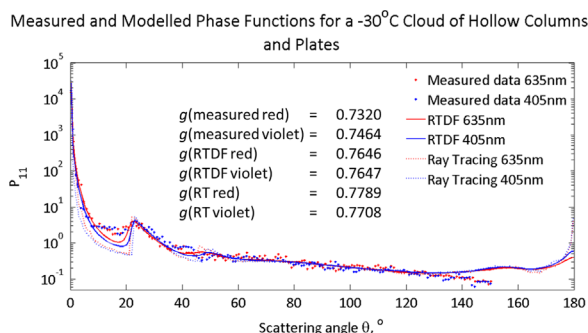


Fig. 18. Measured and modelled phase functions for a cloud of cold hollow columns and hollow plates at  $-30^{\circ}\text{C}$ .

The aspect ratios were measured from the ice crystal replicas. Due to the tendency for plates to land with their basal face parallel to the microscope slide, the aspect ratio of plates was not measured. The measured aspect ratios with respect to maximum particle dimension is given in

Fig. 13. Maximum crystal dimension is defined as  $\sqrt{p^2 + b^2}$ , where  $p$  and  $b$  are the dimensions of the prism and basal facets respectively.

These size distributions and aspect ratios were used to construct habit mixture models for each cloud. For clouds 3 and 4, the aspect ratios could not be measured due to the orientation of the crystals. From CPI images, the thickness of the plates was estimated to be  $15\ \mu\text{m}$ . This thickness was used for all plate sizes. The particle models were used in both RT and RTDF.

#### 4. Discussion

In Figs. 14–18, it can be seen that there are random variations, or noise, in the measured phase functions. This can be attributed, in part, to low signal to noise ratios, where ‘signal’ is defined as the measured intensity, and ‘noise’ is defined as the background intensity. At larger angles where the scattered intensity was weak, typical signal to noise ratios were  $\sim 2$ . As the lasers were diode lasers with inherently short coherence lengths, the noise cannot be attributed to laser speckle. Each experiment was repeated four times in order to gain average measurements. The average signal to noise ratios and standard deviations for all experiments are given in Table 3.

A summary of the measured and modelled asymmetry parameters is given in Table 4.

For cloud 1, solid columns at  $-7^{\circ}\text{C}$ , there is little difference between the asymmetry parameters predicted by Ray Tracing and RTDF. Both RT and RTDF over-predict the asymmetry parameter by 5.2–7.4%. However, differences are easily seen in the phase function (Fig. 14). Compared to measured results, Ray Tracing over-predicts the  $22^{\circ}$  halo and over-predicts scattering in the  $140$ – $150^{\circ}$  range. It also under-predicts scattering in the  $0$ – $10^{\circ}$  range. By comparison, the  $22^{\circ}$  halo predicted by RTDF is smaller and smoother, fitting within the errors of measured results.

For cloud 2, hollow columns at  $-7^{\circ}\text{C}$ , both models over-predict the asymmetry parameter by 6.5–8.5%. The halo feature predicted by Ray Tracing is significantly reduced when compared to the solid column model, however the halo is still sharper than measured results, leading to an under-prediction of scattering in the  $10$ – $20^{\circ}$  range and an over-prediction of scattering in the  $20$ – $30^{\circ}$  range. By comparison, the shape of the halo feature predicted by RTDF is much smoother, although the peak is still over-predicted.

Both plate clouds (clouds 3 and 4) show a significant deviation between the measured and modelled phase functions in the  $120$ – $150^{\circ}$  range. This may be due to the inaccurate modelling of plate particles. As described in Section 3.1, the prism facet of plate habits could not be measured from the formvar replicas. Based on CPI images, it was decided to model all plates with a thickness of  $15\ \mu\text{m}$ . The modelled phase functions all exhibit a trough feature between  $120^{\circ}$  and  $150^{\circ}$ , which is not seen for columnar habits. This deviation may be caused, in part, by the under-prediction of the thickness of the plates. In addition to this, it can be seen from Fig. 12 that the hollow plates produced in cloud 4 had additional features protruding from the prism facets, the particles in cloud 3 had rounded edges, and both clouds contained scalene particles. Omitting these features in the model may cause deviations from the measured results. Comparing the measured results for clouds 3 and 4, we observe a reduction in asymmetry parameter for cloud 4 when compared with cloud 3. However, the modelled results show an increase in asymmetry parameter for cloud 4 when compared to cloud 3. This is due to the change in aspect ratio of the particles. The hollow plate cloud was created at a higher humidity than the solid plate cloud by increasing the vapour input to the chamber. This created the hollow particles as seen in Fig. 12, however the ice crystals also exhibited smaller aspect ratios and therefore they cannot be directly compared.

For cloud 5, hollow columns at  $-30^{\circ}\text{C}$ , there is a significant deviation in the results in the  $140$ – $150^{\circ}$  range. As described with respect to the plate clouds (clouds 3 and 4), this may be due to a none representative selection of the size and aspect ratio of the particles. The particles collected in cloud 5 had typical aspect ratios close to one, and therefore both orientations were seen in the formvar replicas. However, if thin, plate-like particles were present in the cloud, they may have oriented on the microscope slides with their basal facet parallel to the slide. In this

**Table 3**

Average signal to noise ratios (SNR) and standard deviations (as a percentage of the mean) of the intensity measurements used to obtain the phase functions.

Angular range, °	0–10	10–30	30–50	50–70	70–90	90–110	110–130	130–150
SNR	14.32	6.95	5.52	4.31	2.48	2.15	1.98	2.01
Standard deviation, %	4	9	14	17	23	26	24	24

**Table 4**

Measured and modelled asymmetry parameters for all experiments. ‘% Dev.’ gives the percentage deviation of the modelled result from the measured result.

Measurement/Model	Cloud 1		Cloud 2		Cloud 3		Cloud 4		Cloud 5	
	g	% Dev.								
Measured (red)	0.7623		0.7746				0.7779		0.7320	
Measured (violet)	0.7698		0.7825		0.8243		0.7851		0.7464	
RTDF (red)	0.8117	6.48	0.8339	7.66			0.8611	10.70	0.7646	4.45
RTDF(violet)	0.8097	5.19	0.8331	6.47	0.8500	3.13	0.8630	9.93	0.7647	2.45
RT (red)	0.8186	7.40	0.8406	8.52			0.8717	12.05	0.7789	6.41
RT (violet)	0.8119	5.47	0.8352	6.74	0.8490	2.99	0.8677	10.52	0.7708	3.27

case, the aspect ratio could not be measured and was therefore not recorded. Due to this, the range of predicted aspect ratios may have been skewed to larger sizes. There is also a deviation from modelled data in the 10–20° range, which may be caused by particle roughness, which is known to smooth out halo features. Alternatively it could be caused by particles with more numerous indentations. Each indentation is modelled by three steps based on averaged measurements. However, particles with more or less steps have been observed. The presence of additional step features could cause light to leave the particle at shallower angles, causing increased scattering in the 10–20° range.

## 5. Conclusions

The cavities of hollow ice particles were found to have differing structures at different temperatures, and the structure of the cavity was found to influence the single scattering properties of the particles.

In Section 3.1, solid and hollow particle models were tested using RT and RTDF in order to determine the effects of two types of indentation. It was found that the two types of indentations had differing effects. For the hollow particle based on particles seen at  $-7^{\circ}\text{C}$ , both RT and RTDF predict an increase in the asymmetry parameter compared to a solid column of the same aspect ratio 1. For the hollow particle model with the stepped internal structure, both RT and RTDF predict a decrease in asymmetry parameter compared with a solid column of the same aspect ratio. In all cases, RT and RTDF over-predict the asymmetry parameter. As an average across all experiments, RT over-predicts the asymmetry by 6.8%, whereas RTDF over-predicts asymmetry parameter by 6.11%. The phase functions predicted by RT showed more prominent halo features than those predicted by RTDF. Both the hollow particle models caused a reduction in the 46° halo when using the RTDF model, however these features remained prominent when using RT. The phase functions

predicted from RTDF show less deviation from measured results compared with RT, particularly in the halo regions and the forward scattering range.

Due to experimental conditions, roughness and hollowness cannot be entirely separated. In all experiments, it is possible that surface roughness contributed to diminished halo features, which were typically over-predicted by the models. Surface roughness is also known to reduce the asymmetry parameter [45], which may explain the discrepancy between measured and modelled results. Due to this, measured asymmetry parameters from these experiments may be larger than field experiments due to more constrained lab conditions and restricted growth times leading to more pristine particles.

## Acknowledgements

This work was funded by the Natural Environment Research Council (NERC) in conjunction with a CASE studentship from Met Office. We also acknowledge funding from the NERC ACID-PRUF programme, Grant code NE/I020121/1.

## References

- [1] Intergovernmental Panel on Climate Change. The physical science basis: contribution of working group 1 to the fifth assessment report of the IPCC; 2013. Cambridge: Cambridge University Press.
- [2] Zhang Y, Macke A, Albers F. Effect of crystal size spectrum and crystal shape on stratiform cirrus radiative forcing. *Atmos Res* 1999;52:59–75.
- [3] Liou KN, Takano Y. Light scattering by nonspherical particles: remote sensing and climatic implications. *Atmos Res* 1994;31:271–98.
- [4] Baran AJ. From the single-scattering properties of ice crystals to climate prediction: a way forward. *Atmos Res* 2012;112:45–69.
- [5] Sassen K, Wang Z, Liu D. Global distribution of cirrus clouds from CloudSat/Cloud-Aerosol Lidar and Infrared Pathfinder Satellite Observations (CALIPSO) measurements. *J Geophys Res* 2008;113: D00A12.
- [6] Descartes R, Tremblay J-M. (Trans.) The Météors ([www.classiques.uqac.ca/classiques/Descartes/meteores/meteores.html](http://www.classiques.uqac.ca/classiques/Descartes/meteores/meteores.html)); 2002.

- [7] Kepler J. In: On the six cornered snowflake. Oxford: Clarendon; 1966.
- [8] Mason BJ. Snow crystals, natural and man made. *Contemp Phys* 1992;33:227–43.
- [9] Nakaya U. In: Snow crystals: natural and artificial. Harvard University Press; 1954.
- [10] Bailey MP, Hallett J. A comprehensive habit diagram for atmospheric ice crystals: confirmation from the laboratory, AIRS II, and other field studies. *J Atmos Sci* 2009;66:2888–99.
- [11] Bailey M, Hallett J. Growth rates and habits of ice crystals between  $-20\text{ }^{\circ}\text{C}$  and  $-70\text{ }^{\circ}\text{C}$ . *J Atmos Sci* 2004;61:514–44.
- [12] Miloshevich LM, Heymsfield AJ. A balloon-borne continuous cloud particle replicator for measuring vertical profiles of cloud microphysical properties: instrument design, performance, and collection efficiency analysis. *J Atmos Ocean Technol* 1997;14:753–68.
- [13] Barkley B, Bailey M, Liou K-N, Hallett J. Light-scattering properties of plate and column ice crystals generated in a laboratory cold chamber. *Appl Opt* 2002;41:5792–6.
- [14] Rimmer JS, Saunders CPR. Extinction measurements and single scattering albedo in the 0.5 to 1.05  $\mu\text{m}$  range for a laboratory cloud of hexagonal ice crystals. *Atmos Res* 1998;49:177–88.
- [15] Saunders C, Rimmer J, Jonas P, Arathoon J, Liu C. Preliminary laboratory studies of the optical scattering properties of the crystal clouds. *Ann Geophys* 1998;16:618–27.
- [16] Smedley ARD, Webb AR, Saunders CPR. Application of a diode array spectroradiometer to measuring the spectral scattering properties of cloud types in a laboratory. *Atmos Chem Phys* 2007;7:5803–13.
- [17] Weickmann H. Die Eisphase in der Atmosphäre. Farnborough: Royal Aircraft Establishment; 1947.
- [18] Heymsfield A, Miloshevich L. Parameterizations for the cross-sectional area and extinction of cirrus and stratiform ice cloud particles. *J Atmos Sci* 2003;60:936–56.
- [19] Lawson RP, Baker BA, Zmarzly P, O'Connor D, Mo Q, Gayet J-F, et al. Microphysical and optical properties of atmospheric ice crystals at South Pole Station. *J Appl Meteor Clim* 2006;45:1505–24.
- [20] Um J, McFarquhar GM. Single-scattering properties of aggregates of plates. *Q J R Meteorol Soc* 2009;304:291–304.
- [21] Gayet J-F, Mioche G, Bugliaro L, Protat A, Minikin A, Wirth M, et al. On the observation of unusual high concentration of small chain-like aggregate ice crystals and large ice water contents near the top of a deep convective cloud during the CIRCLE-2 experiment. *Atmos Chem Phys* 2012;12:727–44.
- [22] Gallagher MW, Connolly PJ, Whiteway J, Figueras-Nieto D, Flynn M, Choulaton TW, et al. An overview of the microphysical structure of cirrus clouds observed during EMERALD-1. *Q J R Meteorol Soc* 2005;131:1143–69.
- [23] Vogelmann AM, Ackerman TP. Relating cirrus cloud properties to observed fluxes: a critical assessment. *J Atmos Sci* 1995;52:4285–301.
- [24] McFarquhar GM, Yang P, Macke A, Baran AJ. A new parameterization of single scattering solar radiative properties for tropical anvils using observed ice crystal size and shape distributions. *J Atmos Sci* 2002;59:2458–78.
- [25] McFarquhar GM, Heymsfield AJ, Macke A, Iaquinta J, Aulenbach SM. Use of observed ice crystal sizes and shapes to calculate mean-scattering properties and multispectral radiances: CEPEX April 4, 1993, case study. *J Geophys Res* 1999;104:31763.
- [26] Lindqvist H, Muinonen K, Nousiainen T, Um J, McFarquhar GM, Haapanala P, et al. Ice-cloud particle habit classification using principal components. *J Geophys Res* 2012;117:D16206.
- [27] Key JR, Yang P, Baum BA, Nasiri S. Parameterization of shortwave ice cloud optical properties for various particle habits. *J Geophys Res* 2002;107(D13).
- [28] Yang H, Dobbie S, Herbert R, Connolly P, Gallagher M, Ghosh S, et al. The effect of observed vertical structure, habits, and size distributions on the solar radiative properties and cloud evolution of cirrus clouds. *Q J R Meteorol Soc* 2011;0:1–14.
- [29] Macke A, Francis PN, McFarquhar GM, Kinne S. The role of ice particle shapes and size distributions in the single scattering properties of cirrus clouds. *J Atmos Sci* 1998;55:2874–83.
- [30] Bacon NJ, Swanson BD. Laboratory measurements of light scattering by single levitated ice crystals. *J Atmos Sci* 2000;57:2094–104.
- [31] Macke A, Mueller J, Raschke E. Single scattering properties of atmospheric ice crystals. *J Atmos Sci* 1996;53:2813–25.
- [32] Yang P, Liou KN. Geometric-optics-integral-equation method for light scattering by nonspherical ice crystals. *Appl Opt* 1996;35:6568–84.
- [33] Baran AJ, Watts PD, Francis PN. Testing the coherence of cirrus microphysical and bulk properties retrieved from dual-viewing multispectral satellite radiance measurements. *J Geophys Res* 1999;104:31673–83.
- [34] Baran AJ, Labonnote LC. On the reflection and polarization properties of ice cloud. *J Quant Spectrosc Radiat Transf* 2006;100:41–54.
- [35] Macke A, Mishchenko MI. Applicability of regular particle shapes in light scattering calculations for atmospheric ice particles. *Appl Opt* 1996;35:4291–6.
- [36] Gerber H, Takano Y, Garrett TJ, Hobbs PV. Nephelometer measurements of the asymmetry parameter, volume extinction coefficient, and backscatter ratio in arctic clouds. *J Atmos Sci* 2000;57:3021–34.
- [37] Lampert A, Ehrlich A, Dornbrack A, Jourdan O, Gayet J-F, Mioche G, et al. Microphysical and radiative characterization of a subsvisible midlevel Arctic ice cloud by airborne observations—a case study. *Atmos Chem Phys* 2009;9:2647–61.
- [38] Gayet J-F, Mioche G, Shcherbakov V, Gourbeyre C, Busen R, Minikin A. Optical properties of pristine ice crystals in mid-latitude cirrus clouds: a case study during CIRCLE-2 experiment. *Atmos Chem Phys* 2011;11:2537–44.
- [39] Garrett TJ, Gerber H, Baumgardner DG, Twohy CH, Weinstock EM. Small, highly reflective ice crystals in low-latitude cirrus. *Geophys Res Lett* 2003;30(21):2132.
- [40] Garrett TJ, Navarro BC, Twohy CH, Jensen EJ, Baumgardner DG, Bui PT, et al. Evolution of a Florida cirrus anvil. *J Atmos Sci* 2005;62:2352–72.
- [41] Van Diedenhoven B, Cairns B, Fridlind AM, Ackerman AS, Garrett TJ. Remote sensing of ice crystal asymmetry parameter using multi-directional polarization measurements—Part 2: application to the research scanning polarimeter. *Atmos Chem Phys* 2013;13:3185–203.
- [42] Yang P, Hong G, Kattawar G, Minnis P, Hu Y. Uncertainties associated with the surface texture of ice particles in satellite-based retrieval of cirrus clouds: Part II—effect of particle surface roughness on retrieved cloud optical thickness and effective particle size. *IEEE Trans Geosci Remote Sens* 2008;46(7):1948–57.
- [43] Schmitt CG, Heymsfield AJ. On the occurrence of hollow bullet rosette- and column-shaped ice crystals in midlatitude cirrus. *J Atmos Sci* 2007;64:4514–9.
- [44] Neshyba SP, Lowen B, Benning M, Lawson A, Rowe PM. Roughness metrics of prismatic facets of ice. *J Geophys Res* 2013;118:3309–18.
- [45] Ulanowski Z, Kaye PH, Hirst E, Greenaway RS, Cotton RJ, Hesse E, et al. Incidence of rough and irregular atmospheric ice particles from Small Ice Detector 3 measurements. *Atmos Chem Phys* 2014;14:1622–49.
- [46] Shcherbakov V, Gayet J-F, Baker BA, Lawson RP. Light scattering by single natural ice crystals. *J Atmos Sci* 2006;63:1513–25.
- [47] Shcherbakov V, Gayet J-F, Jourdan O, Ström J, Sinikin A. Light scattering by single ice crystals of cirrus clouds. *Geophys Res Lett* 2006;33:L15809.
- [48] Yang P, Liou K-N. Single-scattering properties of complex ice crystals in terrestrial atmosphere. *Contr Atmos Phys* 1998;71:223–48.
- [49] Liu C, Panetta RL, Yang P. The effects of surface roughness on the scattering properties of hexagonal columns with sizes from the Rayleigh to the geometric optics regimes. *J Quant Spectrosc Radiat Transf* 2013;129:169–85.
- [50] Pfalzgraff WC, Hulscher RM, Neshyba SP. Scanning electron microscopy and molecular dynamics of surfaces of growing and ablating hexagonal ice crystals. *Atmos Chem Phys* 2010;10:2927–35.
- [51] Schnaiter M, Kaye PH, Hirst E, Ulanowski Z, Wagner R. Exploring the surface roughness of small ice crystals by measuring high resolution angular scattering patterns. *AAPP* 2011;89(1):5–8.
- [52] Schmitt CG, Iaquinta J, Heymsfield AJ, Iaquinta J. The asymmetry parameter of cirrus clouds composed of hollow bullet rosette-shaped ice crystals from ray-tracing calculations. *J Appl Meteor Clim* 2006;45:973–81.
- [53] Yang P, Zhang Z, Kattawar GW, Warren SG, Baum BA, Huang H-L, et al. Effect of cavities on the optical properties of bullet rosettes: implications for active and passive remote sensing of ice cloud properties. *J Appl Meteor Clim* 2008;47:2311–30.
- [54] Heymsfield AJ, Bansemer A, Field PR, Durden SL, Stith JL, Dye JE, et al. Observations and parameterizations of particle size distributions in deep tropical cirrus and stratiform precipitating clouds: results from in-situ observations in TRMM field campaigns. *J Atmos Sci* 2002;59:3457–91.
- [55] Mason BJ. In: The physics of clouds. Oxford: Clarendon Press; 1957.
- [56] Connolly PJ, Emersic C, Field PR. A laboratory investigation into the aggregation efficiency of small ice crystals. *Atmos Chem Phys* 2012;12:2055–76.

- [57] Rimmer JS, Saunders CPR. Radiative scattering by artificially produced clouds of hexagonal plate ice crystals. *Atmos Res* 1997;45: 153–64.
- [58] Libbrecht KG. The physics of snow crystals. *Rep Prog Phys* 2005;68: 855–95.
- [59] Connolly PJ, Flynn MJ, Ulanowski Z, Choulaton TW, Gallagher MW, Bower KN. Calibration of the Cloud Particle Imager probes using calibration beads and ice crystal analogs: the depth of field. *J Atmos Ocean Technol* 2007;24:1860–79.
- [60] Vaughan G, Bower K, Schiller C, MacKenzie AR, Peter T, Schlager H, et al. SCOUT-O3/ACTIVE: high-altitude aircraft measurements around deep tropical convection. *Bull Am Meteor Soc* 2008;89: 647–62.
- [61] Protat A, McFarquhar GM, Um J, Delano J. Obtaining best estimates for the microphysical and radiative properties of tropical ice clouds from TWP-ICE in situ microphysical observations. *J Appl Meteor Clim* 2011;50:895–915.
- [62] Griggs DJ, Jayarante ER. The replication of ice crystals using formvar: techniques and precautions. *J Atmos Ocean Technol* 1986;3:547–51.
- [63] Platt CMR. Lidar backscatter from horizontal ice crystal patterns. *J Appl Meteor* 1978;17:482–8.
- [64] Chepfer H, Brogniez G, Goloub P, Breon FM, Flamant PH. Observations of horizontally oriented ice crystals in cirrus clouds with POLDER-1/ADEOS-1. *J Quant Spectrosc Radiat Transf* 1999;63: 521–43.
- [65] Heymsfield AJ, Westbrook CD. Advances in the estimation of ice particle fall speeds using laboratory and field measurements. *J Atmos Sci* 2010;67:2469–84.
- [66] van de Hulst HC. In: *Light scattering by small particles*. New York: John Wiley Sons; 1957.
- [67] Hesse E, McCall D, Ulanowski Z, Stopford C, Kaye PH. Application of RTDF to particles with curved surfaces. *J Quant Spectrosc Radiat Transf* 2009;110:1599–603.
- [68] Warren SG, Brandt RE. Optical constants of ice from the ultraviolet to the microwave: a revised compilation. *J Geophys Res* 2008;113: D14220.